Multifunctional Vanadium-doped Cobalt Oxide Layer on Silicon Photoanodes for Efficient and Stable Photoelectrochemical Water Oxidation

Zhuo Xing[a], Hengyi Wu[a], Liang Wu[a], Xuening Wang[a], Huizhou Zhong[a], Feng Li[b], Jinchao Shi[b], Dengyuan Song[b], Wei Xiao[c], Changzhong Jiang[a], Feng Ren[a*].

The Incident Photon-to-Current Efficiency (IPCE) of PEC cell

IPCE was measured in a same three-electrode cell in PEC measurements, using a Newport Tunable light source (300 W Xe source) system with the Cornerstone 130 1/8 m Monochromator. The wavelength scan range is from 300 to 1100 nm, and the scanning was set to 10 nm/step with 5 s for measurement. The intensity of monochromatic light was recorded by Newport Power Meter (Model: 2936-R) with 884-UVR detector that placed at the location of working electrode. The p^+nSi/CoO and $p^+nSi/CoVO$-2 were used as the working electrodes in the three-electrode cell at 1.23 V vs. RHE in 1.0 M KOH. IPCE can be calculated as follows:

$$IPCE = \frac{hcI_{ph,\lambda}}{e\ P_{\lambda}\lambda}$$

where *h, c,* and *e* are the Planck's constant, speed of light in vacuum, and elementary charge, respectively. $I_{ph,\lambda}$ is the photocurrent density, P_{λ} is the power intensity of light, and λ is the wavelength of light.

Electrochemical Impedance Spectroscopy (EIS) Measurements

The EIS spectra for p^+nSi/CoO and $p^+nSi/CoVO$ electrodes in 1.0 M KOH were performed at open-circuit potential (OCP) from the frequency range of 0.1 to 10^5 Hz with 5 mV amplitude. The EIS spectrum was fitting by the Zsimpwin software and the fitted model as follows[1]:

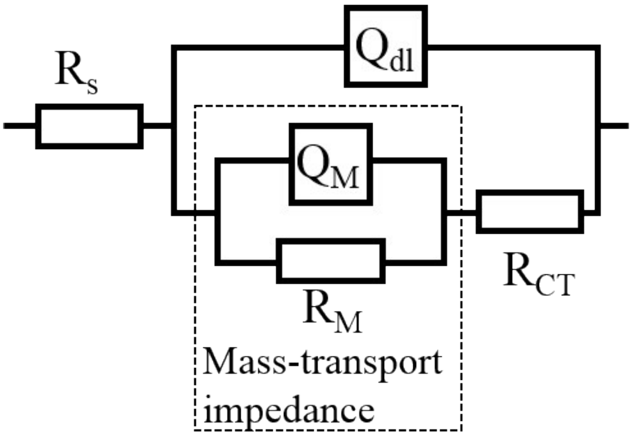

where, R_s is series resistance, R_M is the resistance of LDH, R_{CT} is the charge transfer resistance. Q_{dl} and Q_M model the capacitive behavior of the double layer replacing the infrequently ideal capacitance and diffusion behavior of the double layer and layered double hydroxide (LDH) structure, respectively. The components in dash line box represent modified Mass-transport impedance element. The capacitance (Q) represents a resistance (R), when the dispersion coefficient (n) is equal to 0; Q represents Warburg resistance (W), when n = 0.5; Q represents a capacitance (C), when n = 1; Q represents an inductor (L), when n = -1.

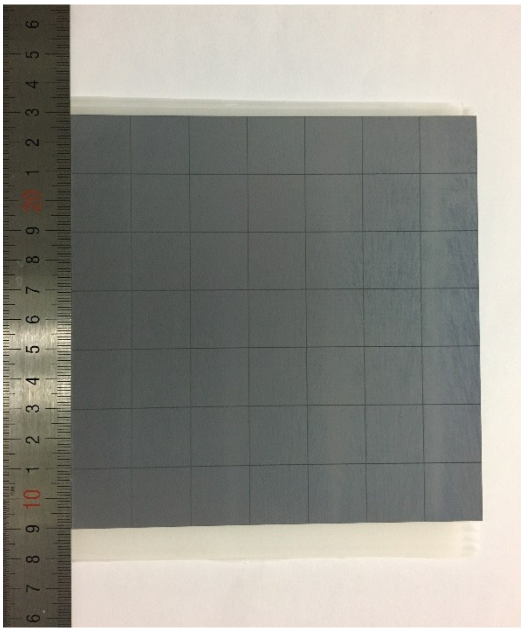

Fig. S1. The scale of p$^+$nSi cell. It was cut into 49 small pieces (2 × 2 cm^2) by laser scribing apparatus.

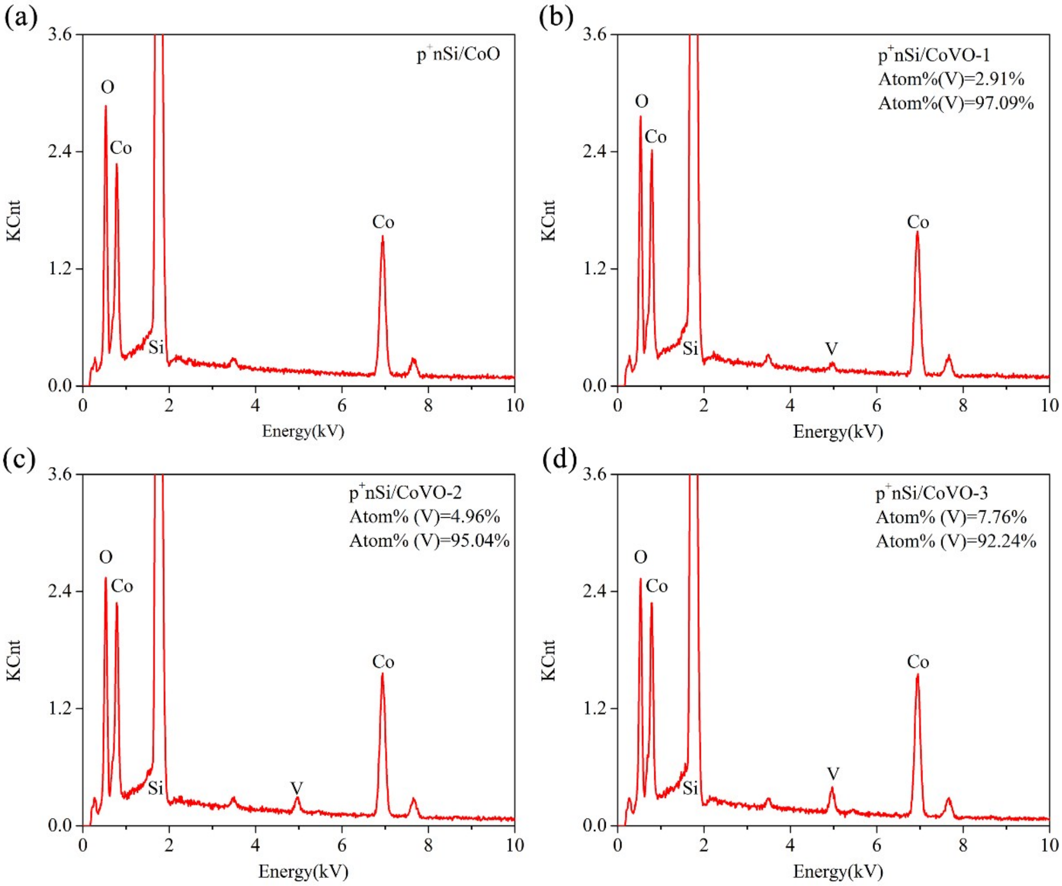

Fig. S2. EDX spectra of p$^+$nSi/CoO, p$^+$nSi/CoVO-1, -2 and -3 with extended depositing time of 14000 s. All of the data collecting time are 110 s.

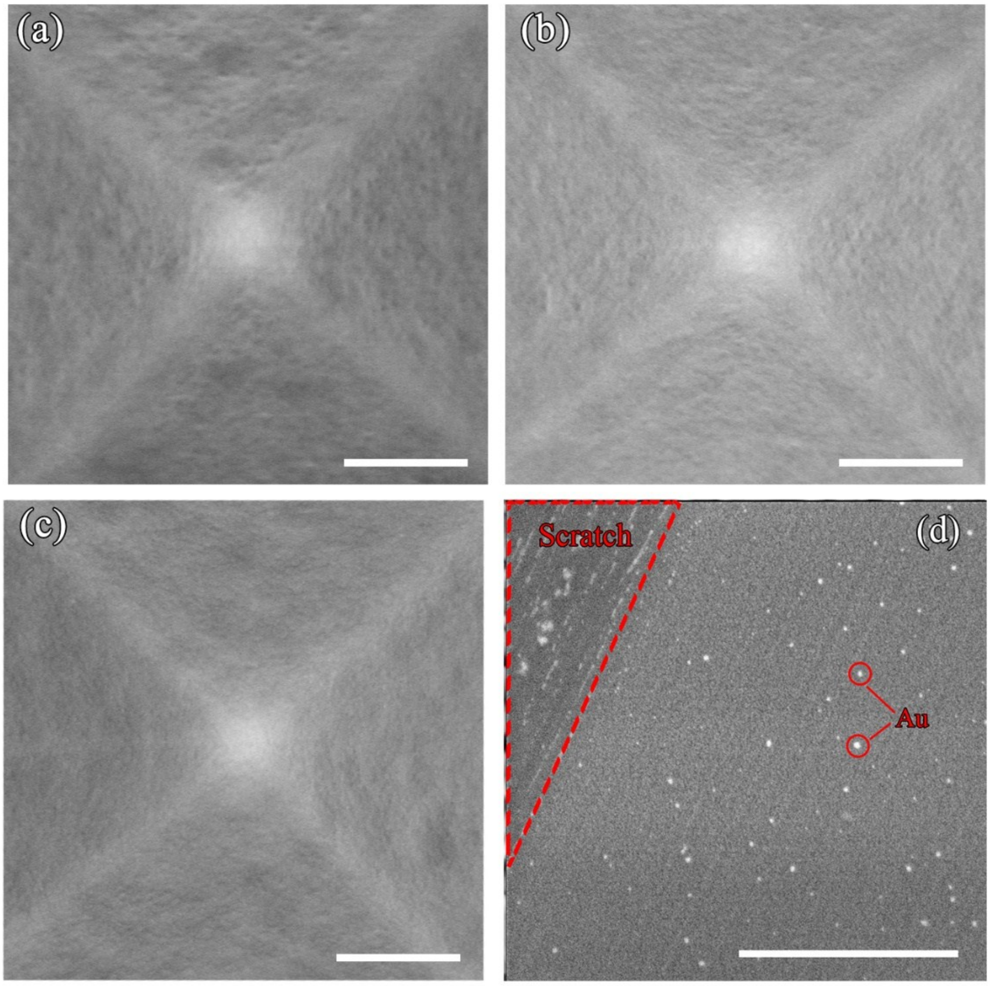

Fig. S3. The planar SEM images of p$^+$nSi/CoO (a), p$^+$nSi/CoVO-1 (b) and -3 (c) and (Co+V)O$_x$ film on the SiO$_2$ substrate (d), the scale bar is 400 nm. Due to the insulation of SiO$_2$ substrate, a thin layer of Au was coated. A scratch was made to increase the contrast of the (Co+V)O$_x$ film which is very flat and uniform.

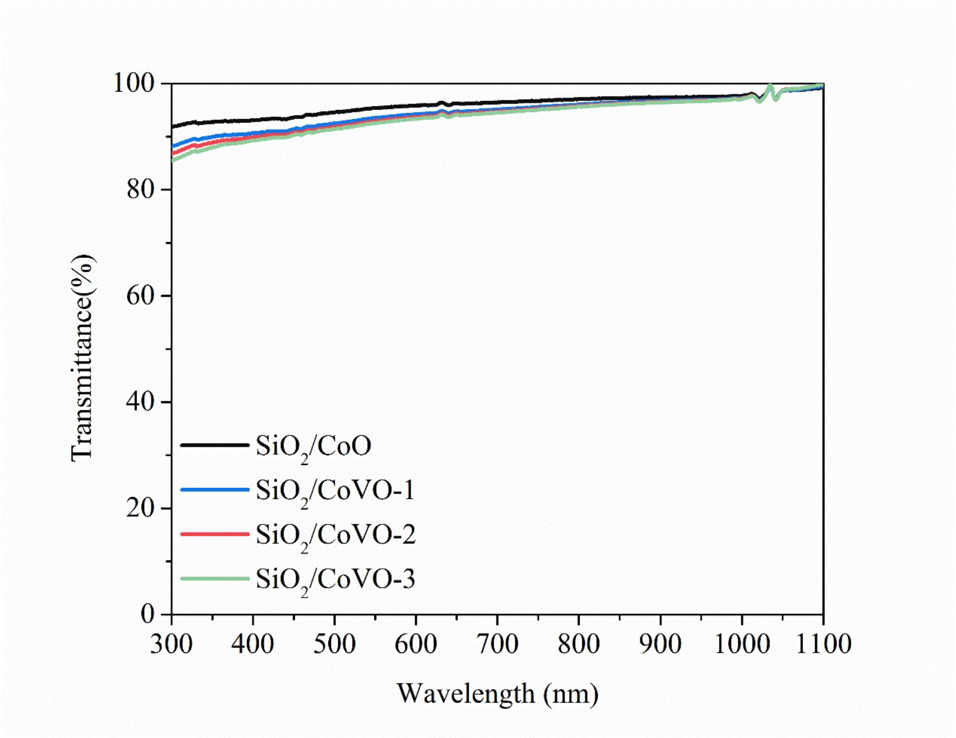

Fig. S4. Optical transmissivity spectra of SiO_2/Co_3O_4, SiO_2/CoVO-1, -2, and -3.

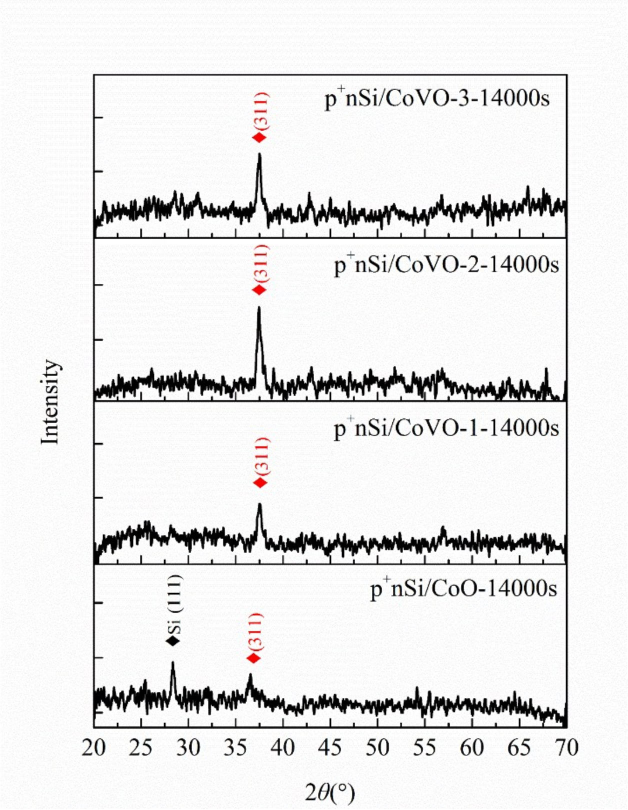

Fig. S5. GIXRD patterns of p^+nSi/CoO, p^+nSi/CoVO-1, -2 and -3 with extended depositing time of 14000 s.

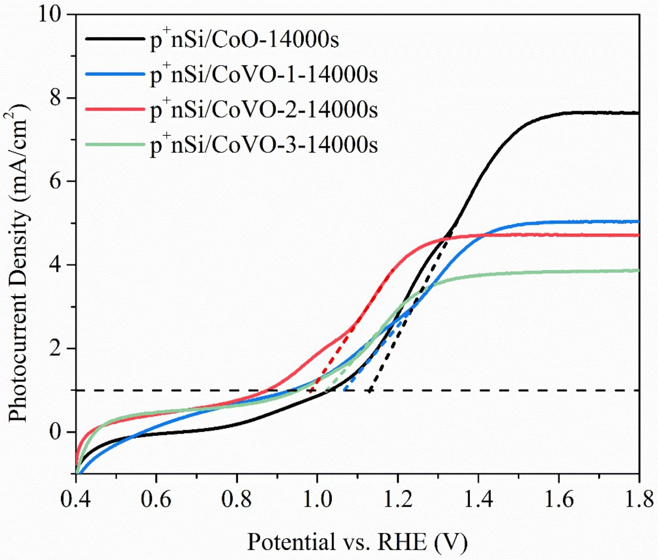

Fig. S6. *J-E* curves of p^+nSi/CoO, $p^+nSi/CoVO$-1, -2 and -3 with extended depositing time of 14000 s. Due to the disturbance of redox peaks, the tangent dash lines are for the eye guide.

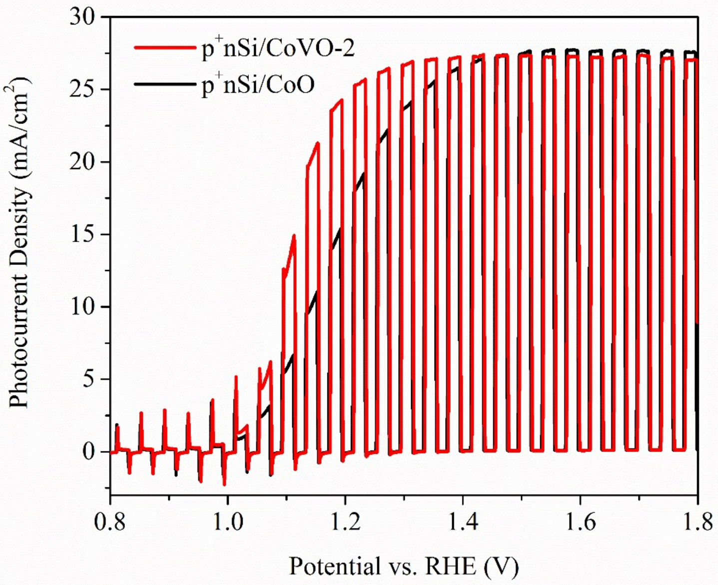

Fig. S7. *J-E* curves of p^+nSi/CoO and $p^+nSi/CoVO$-2 with shutter illumination.

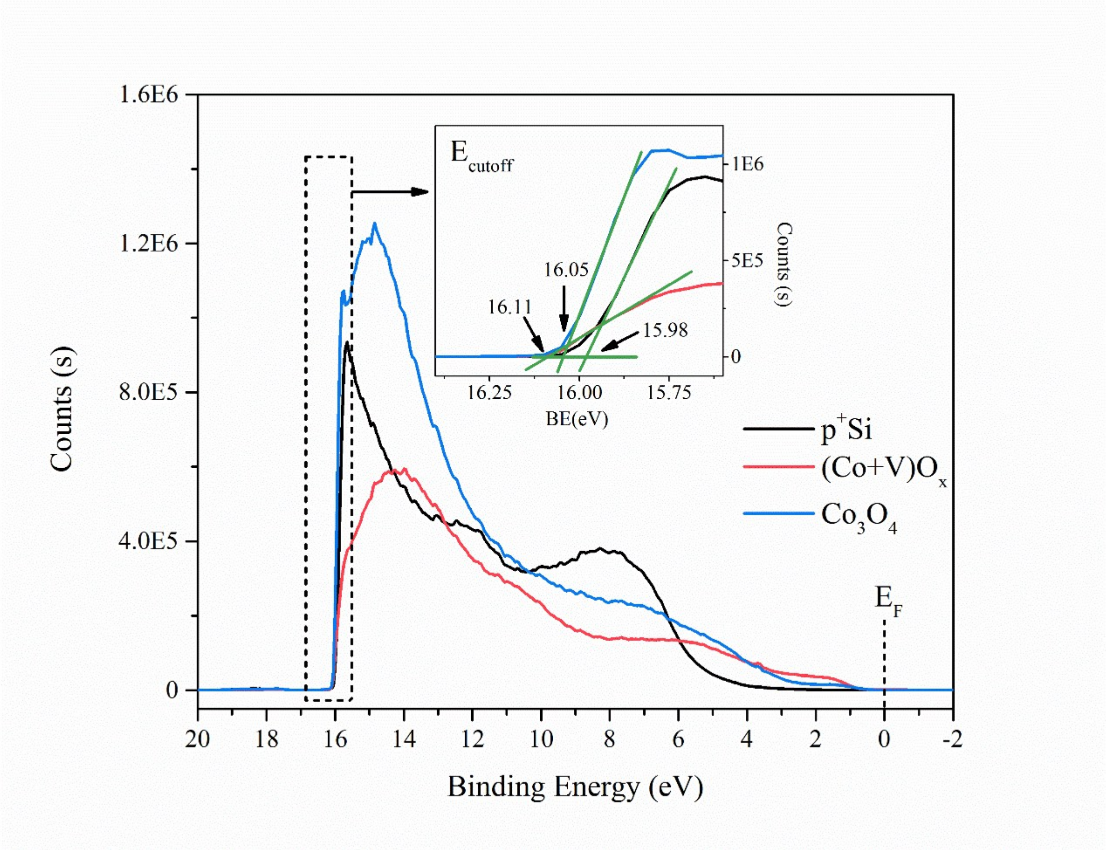

Fig. S8. UPS spectra of p$^+$Si, (Co+V)O$_x$ and Co$_3$O$_4$. The work function is calculated as following:

$$W = h\nu - (E_{Cutoff} - E_F)$$

where, hν is the energy of He I$_\alpha$ (21.22 eV), E_F is the Fermi level of samples, which is equals to 0 eV here. $E_{Cuttoff}$ is the intercept of the baseline. Hence, the work function of p$^+$Si, (Co+V)O$_x$ and Co$_3$O$_4$ are 5.24, 5.11 and 5.17 eV, respectively.

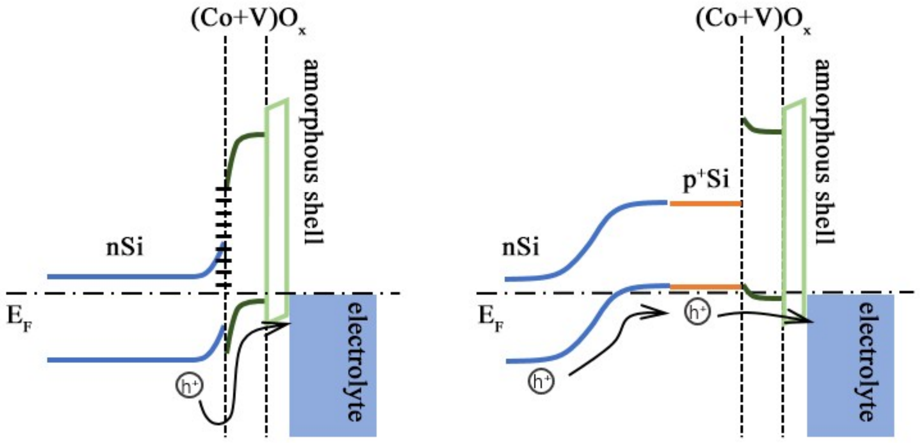

Fig. S9. Energy band diagrams of nSi/CoVO and p$^+$nSi/CoVO photoanodes in 1 M KOH electrolyte (pH = 14).

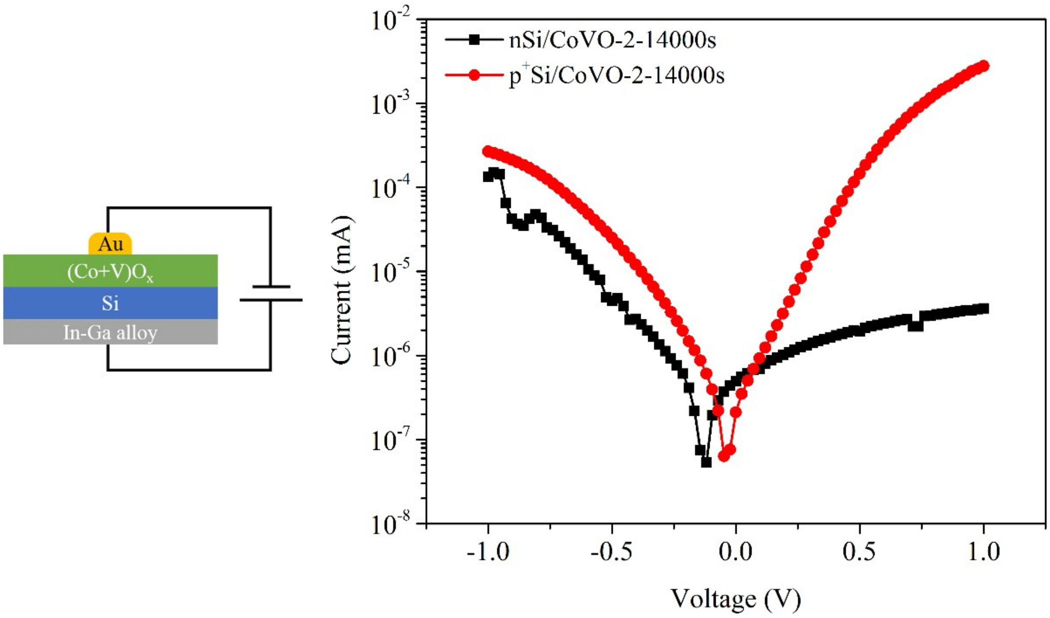

Fig. S10. Electrical measurements of nSi/CoVO-2-14000s and p$^+$Si/CoVO-2-14000s heterojunction: (a) shows the measurement geometry and (b) shows semilog plots of the current in the dark. The current of nSi/CoVO-2-14000s is much smaller than that of p$^+$Si/CoVO-2-14000s at positive voltage, which demonstrates there is a hole extraction barrier between nSi and the (Co+V)O$_x$ film and a good hole transportation for holes between p$^+$Si and the (Co+V)O$_x$ film at positive potential.

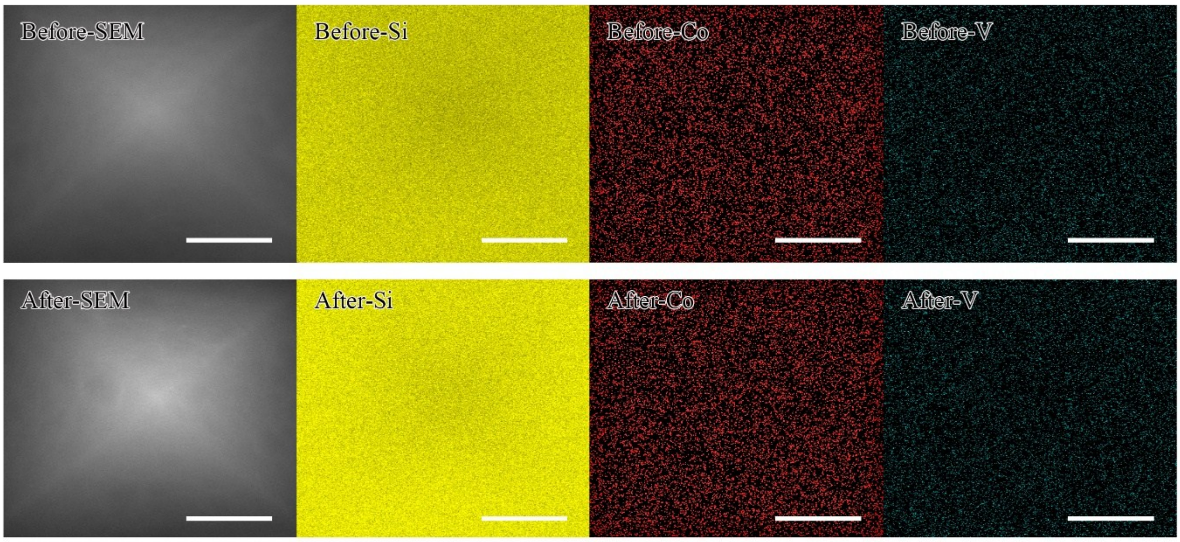

Fig S11. SEM images of p$^+$nSi/CoVO-2 and corresponding EDX mapping of Si, Co, and V before and after 3 h stability test, respectively. The scale bar is 400 nm.

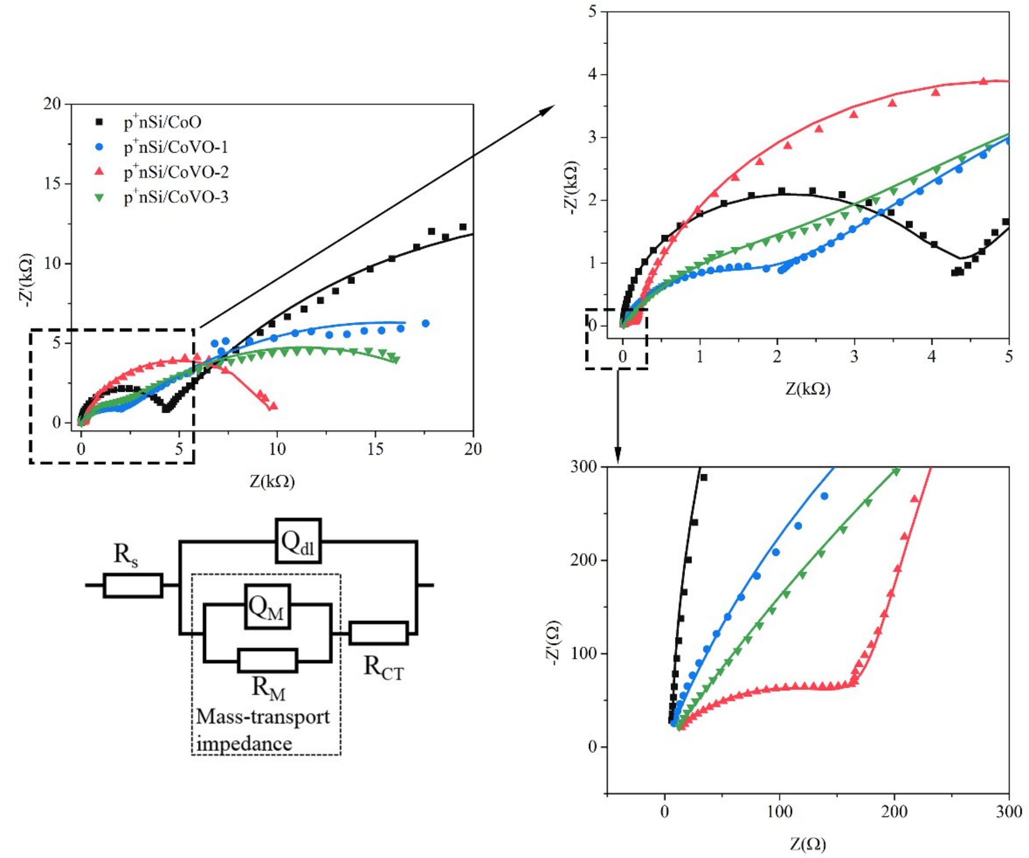

Fig. S12. EIS spectra of p$^+$nSi/CoO, p$^+$nSi/CoVO-1, -2, and -3 in the dark, the corresponding solid lines are fitting lines, which are using the modified Randles circuit shown in the inset.

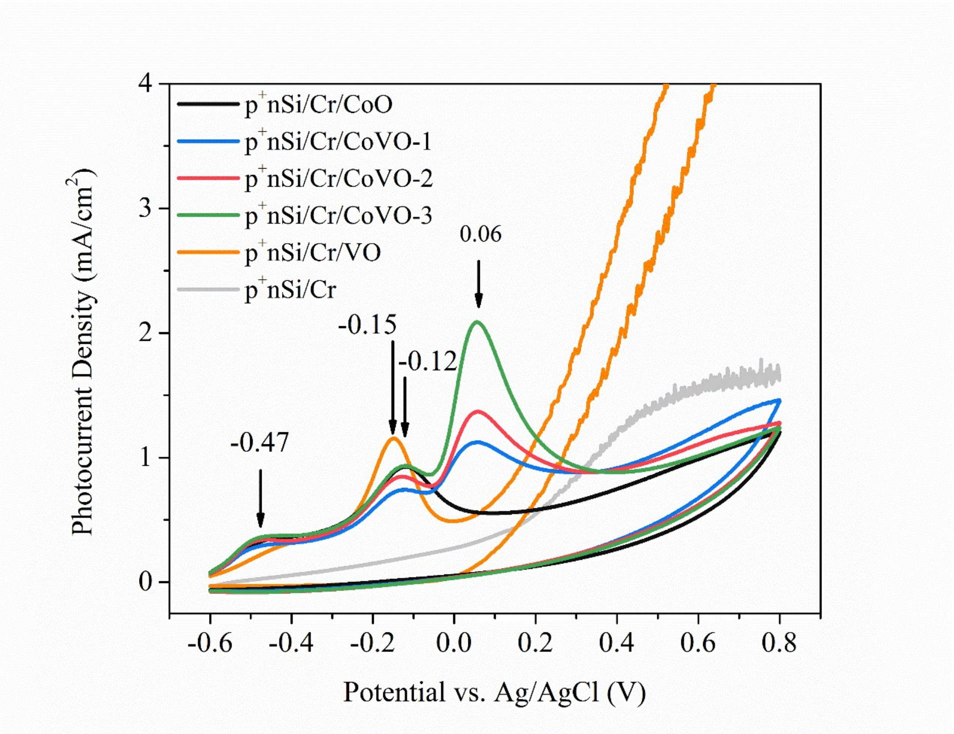

Fig. S13. *J-E* curves of p$^+$nSi/Cr and cyclic voltammetry (CV) curves of p$^+$nSi/Cr/Co_3O_4, p$^+$nSi/Cr/VO,

$p^+nSi/Cr/CoVO$-1, -2, and -3 under illumination with scan rate of 50 mV/s. Note that the peaks at -0.47 and -0.12 V are assigned to Co, and the peaks at -0.15 and 0.06 V are assign to V. The 2nm Cr film between p^+nSi and protection layer can restrict the holes transfer to participate oxygen evolution reaction (OER) and without influence of the intrinsic redox of the atoms in the films. The redox peak at -0.47 V vs Ag/AgCl of $p^+nSi/Cr/CoO$ and $p^+nSi/Cr/CoVO$ indicates that the transformation of Co(II) to Co(III) is a spontaneous process in the $(Co+V)O_x$ film with the help of photovoltage in p^+nSi.

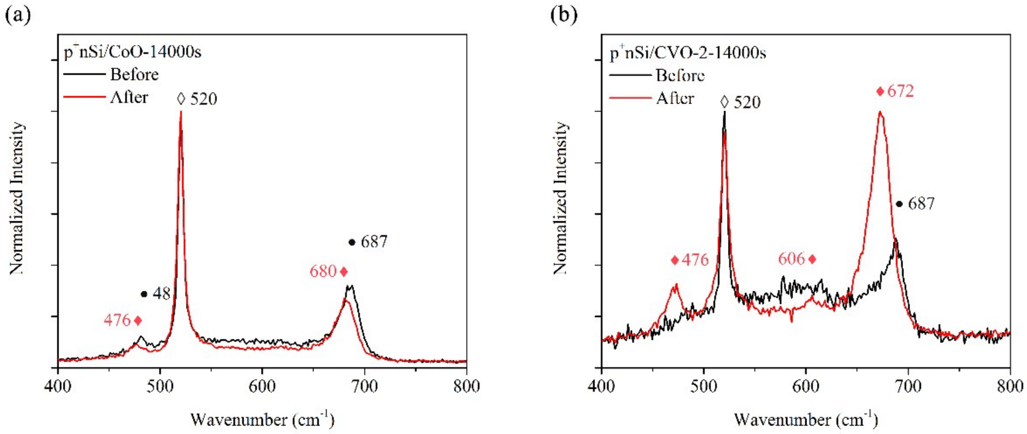

Fig. S14. Raman spectra of p^+nSi/CoO (a) and $p^+nSi/CoVO$-2 (b) with extended depositing time of 14000 s before and after OER. The peak at 520 cm^{-1} is assigned to Si. The characteristic peaks at 481 and 687 cm^{-1} are agree with the E_g and A_{1g} vibration modes of Co_3O_4 (481 and 686 cm^{-1}), respectively.[2] The peaks at 476 and 606 cm^{-1} are assigned to CoOOH.[3, 4] And the wavenumber shift from 687 to 680 or 672 cm^{-1} is attribute to the CoOOH, due to characteristic peak of CoOOH at 675 cm^{-1}.[4]

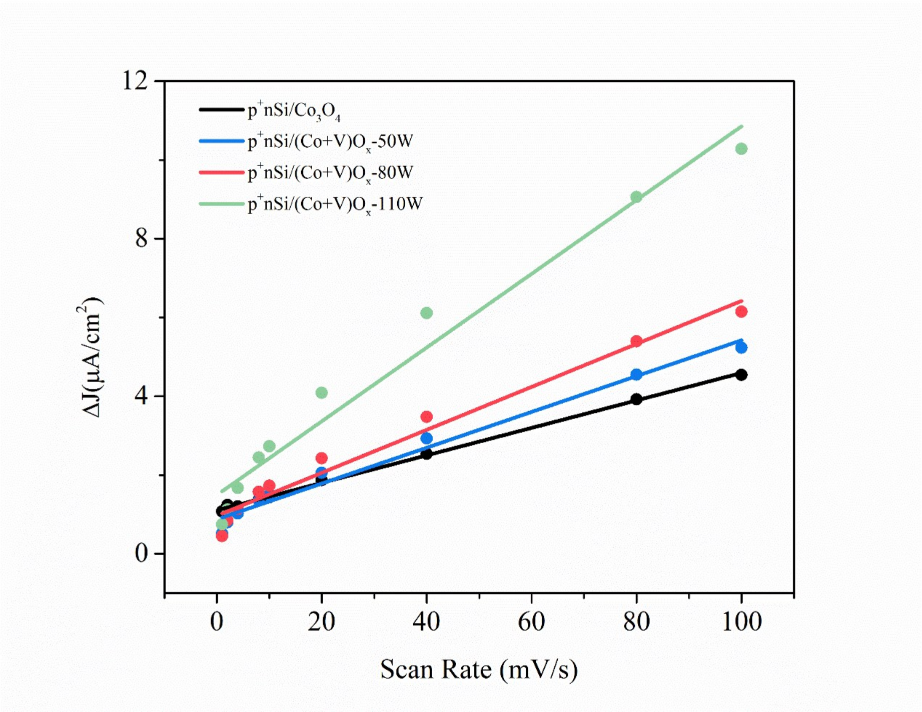

Fig. S15. The electrochemically active surface area (ECSA) of p$^+$nSi/CoO, p$^+$nSi/CoVO-1, -2 and -3, respectively. The measurements range of ECSA is typically a 0.1 V potential window centered at the OCP of the system. The non-Faradaic capacitive current associated with double-layer charging against the scan-rate (1, 2, 4, 8, 10, 20, 40, 80, and 100 mV/s) dependence of corresponding CVs. ECSA is estimated from the double-layer capacitance, which reveals the adsorption of additional hydroxyl at active sites. [5]

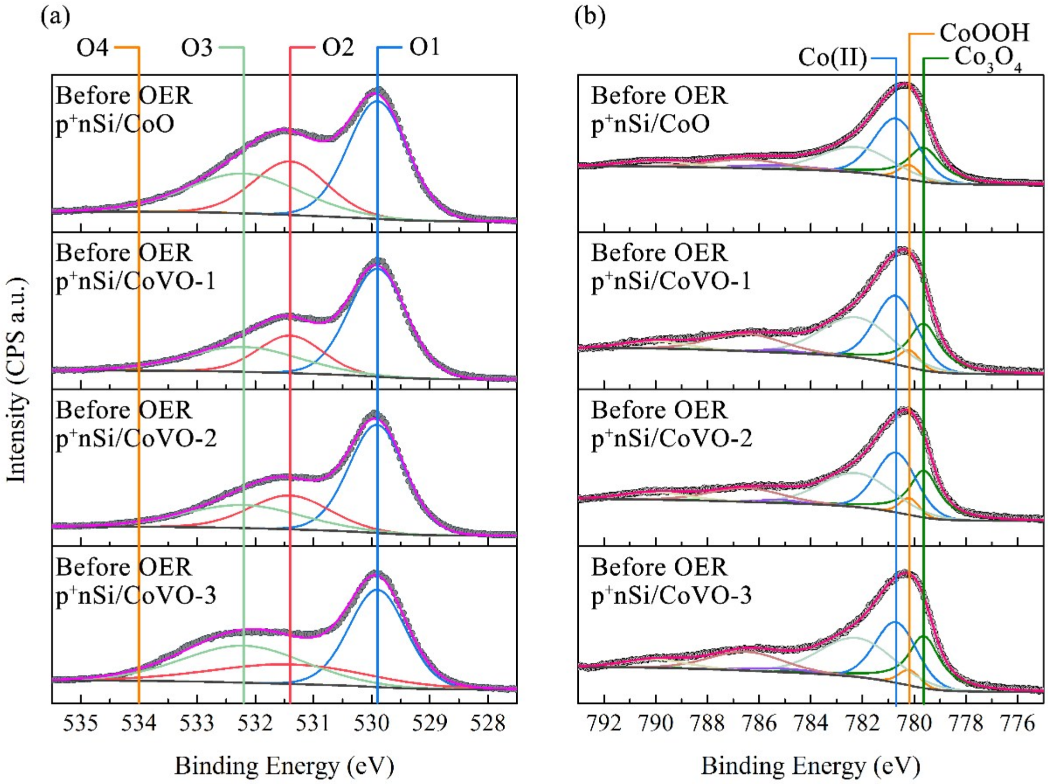

Fig. S16. XPS spectra of (a) O 1s and (b) Co 2p in p$^+$nSi/CoO, p$^+$nSi/CoVO-1, -2 and -3 before OER. However, owning to the shakeup, plasmon loss and Coster−Kronig effects induced spectral broadening, the 2p core-level spectra of first-row transition metals usually exhibit complex asymmetric lines. Hence, a part of constraint models reported in the work of Biesinger et al.[6] was referred to get satisfied fitting.

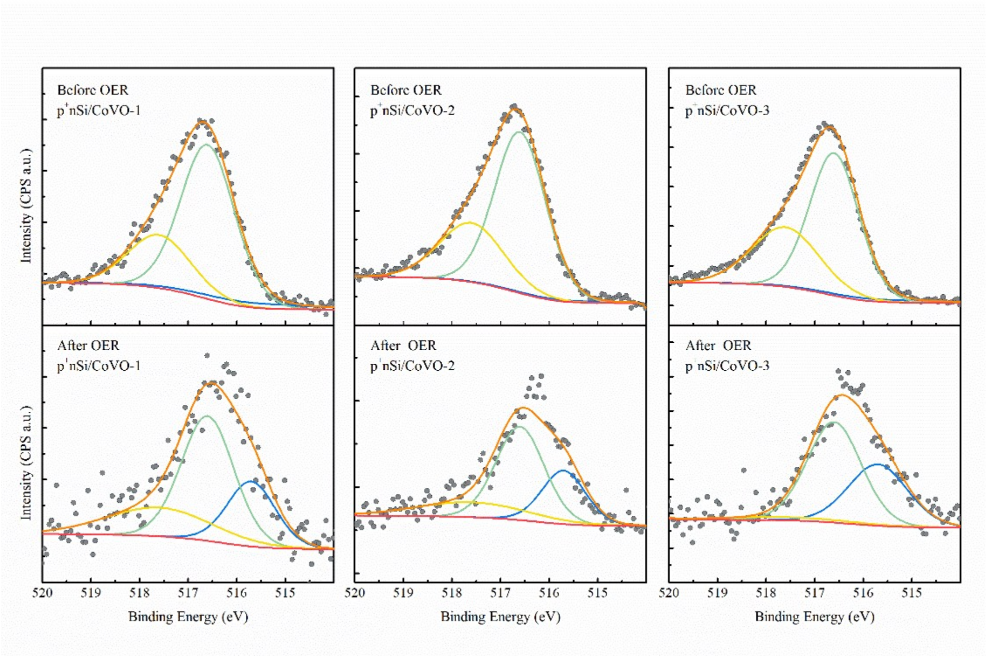

Fig. S17. XPS spectra of V 2p in p$^+$nSi/CoVO-1, -2 and -3 before and after OER.

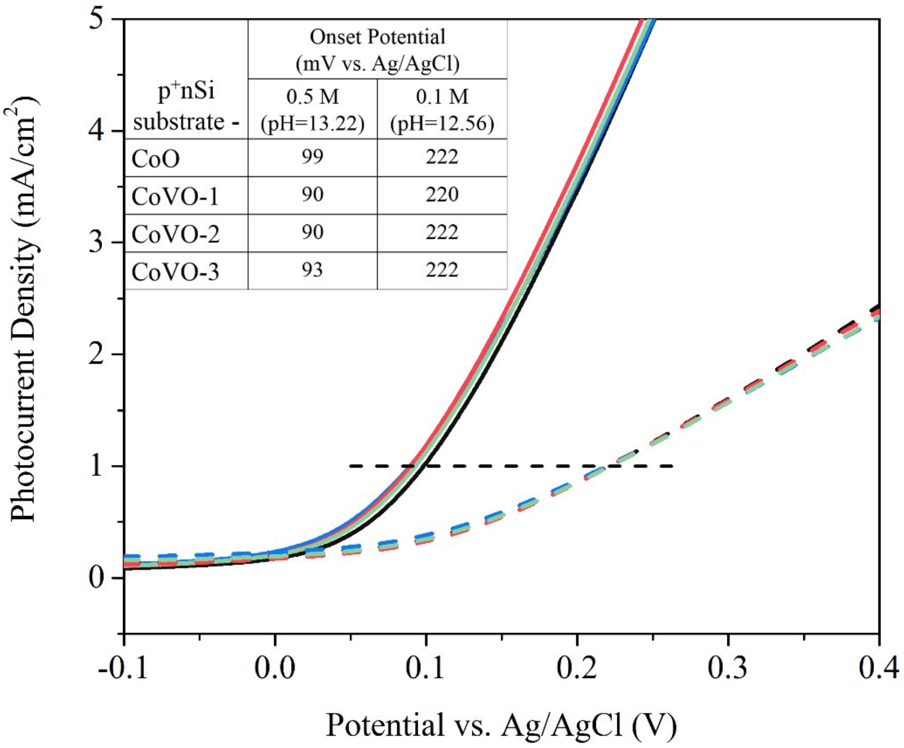

p$^+$nSi substrate -	Onset Potential (mV vs. Ag/AgCl)	
	0.5 M (pH=13.22)	0.1 M (pH=12.56)
CoO	99	222
CoVO-1	90	220
CoVO-2	90	222
CoVO-3	93	222

Fig. S18. *J-E* curves of p$^+$nSi/CoO (black), p$^+$nSi/CoVO-1 (blue), -2 (red), and -3 (green) in 0.5 (solid line) and 0.1 M (dash line) TMAOH with scan rate of 10 mV/s, the inset is the Table of corresponding onset potential.

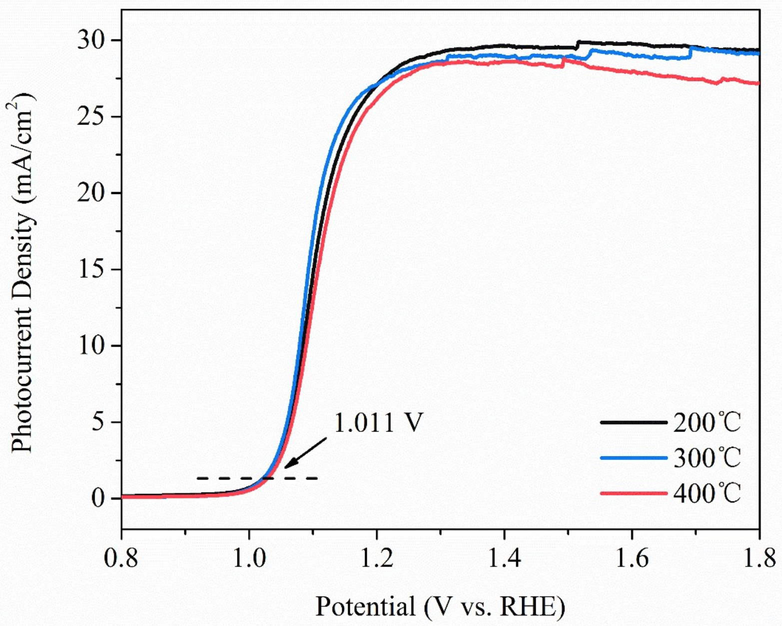

Fig. S19. *J-E* curves of p$^+$nSi /CoO with vacuum-annealing in 200, 300 and 400 ℃ for 1h. The *J-E* curves of p$^+$nSi/CoVO after vacuum annealing show that the onset potential is decrease to 1.011 V, and the different temperature of vacuum annealing doesn't induce notable change of the onset potential. In the process of co-sputtering deposition of Co and V, it is hard to merely increase the content of V without introducing dispensable O vacancies, and the onset potential can' t be further improved by simply managing the concentration of O vacancies. Hence, we prefer to that the doped V is the main factor in the facilitation of generating oxo-bridged Co^{IV}=O in OER.

Table S1. Comparison of the OER activity of p^{+}nSi/CoVO to other PEC cells with p^{+}nSi or nSi substrates in 1 M KOH.

* Data are obtained from digital Fig.s of the references.

	Onset potential vs. RHE (V)	Photocurrent Density (at 1.23 V vs. RHE) (mA/cm^2)	Reference
p^{+}nSi/CoVO	1.000	29.13	This work
p^{+}nSi/CoO/$Co(OH)_2$	1.007*	30.8	Nat. Mater. 16 (2017) 335.[7]
nSi/SiO_x/Ni@$Ni(OH)_2$	1.030	15.5	ChemSusChem. 10 (2017) 2897.[8]
nSi/ TiO_2/$Ni_{80}Fe_{20}$	1.060	21.5	ACS Catalysis. 7 (2017) 3277.[9]
nSi/SiO_x/CoO_x	1.018	23.2	Energy Environ. Sci. 9 (2016) 892.[10]
nSi/TiO_x/ITO/NiOOH	0.900	18	JACS. 138 (2016) 13664.[11]
p^{+}nSi/$NiCo_2O_4$	0.950	26	JACS. 137 (2015) 9595.[12]
p^{+}nSi/NiO_x	1.030	29	J. Phys. Chem. Lett. 6 (2015) 592.[13]
p^{+}nSi/CoO	1.010*	17	JACS. 136 (2014) 6191.[14]
p^{+}nSi/Ni/NiO_x-Fe-treated	1.070*	17*	J. Phys. Chem. Lett. 5 (2014) 3456.[15]
p^{+}nSi/TiO_2/Ni	1.118*	27.7	Science. 344 (2014) 1005.[16]

Table S2. Electron binding energies (eV) and relative contents of atom % for several peak fitting of the Co 2p, O 1s, and V 2p lines before and after OER.

		Co 2p			O 1s				V 2p		
		Co_3O_4	CoOOH	Co (II)	O1	O2	O3	O4	V1	V2	V3
	eV	779.6	780.18	780.07	529.9	531.4	532.2	534	515.7	516.6	517.6
Before OER p$^+$nSi/CoO	%	35.32	6.63	58.05	45.23	25.35	29.06	0.36			
Before OER p$^+$nSi/CoVO-1	%	38.84	6.64	54.52	54.25	21.16	24.34	0.24	5.34	67.6	27.06
Before OER p$^+$nSi/CoVO-2	%	41.53	6.97	51.49	52.84	23.59	23.51	0.05	1.53	67.4	31.07
Before OER p$^+$nSi/CoVO-3	%	45.03	6.26	48.71	42.55	23.13	34.32	0	2.8	61.77	35.43
After OER p$^+$nSi/CoO	%	42.71	23.82	33.48	10.16	35.2	52.9	1.74			
After OER p$^+$nSi/CoVO-1	%	28.38	49.79	21.84	20.35	43.66	34.27	1.72	6.08	56.03	37.89
After OER p$^+$nSi/CoVO-2	%	27.17	55.4	17.43	19.71	47.62	31.46	1.21	27.3	53.02	19.68
After OER p$^+$nSi/CoVO-3	%	21.93	68.61	9.45	23.24	46.91	28.57	1.27	38.13	57.23	4.64

Table S3. The nomenclature of samples and corresponding substrates, protecting films, thicknesses of protecting film and measurements.

	Substrate	Protecting Film		Thickness of Protecting Film	Measurements
p+nSi/Cr/VO	2 nm Cr coated p^+nSi	VO_x		2 nm	*J-E* curve (Fig. S13)
p^+nSi/Cr					CV curve (Fig. S13)
p^+nSi/Cr/CoO		Co_3O_4		70 nm	
p^+nSi/Cr/CoVO-1		2.91 % V doped	$(Co+V)O_x$		
p^+nSi/Cr/CoVO-2		4.96% V doped			
p^+nSi/Cr/CoVO-3		7.76 % V doped			
SiO_2/CoO	SiO_2	Co_3O_4			Transmissivity spectra (Fig. S4)
SiO_2/CoVO-1		2.91 % V doped	$(Co+V)O_x$		
SiO_2/CoVO-2		4.96% V doped			
SiO_2/CoVO-3		7.76 % V doped			
nSi/CoVO-2	nSi	4.96% V doped	$(Co+V)O_x$		*J-E* curve (Fig. 2b)
p^+Si/CoVO-2	p^+Si				

p^+nSi/CoO	p^+nSi	Co_3O_4		70 nm	*J-E* curve (Fig. 2a, 3c, 5, S7, S18), IPCE (Fig. 2c), EIS (Fig. 3a), OCP (Fig. 3b), XPS (Fig. 4, S16, Table S2), SEM (Fig. S3), ECSA (Fig. S15)
p^+nSi/CoVO-1		2.91 % V doped	$(Co+V)O_x$		*J-E* curve (Fig. 2a, 3c, 5, S18), EIS (Fig. 3a, S12), OCP (Fig. 3b), XPS (Fig. 4, S16, S17, Table S2), ECSA (Fig. S15)
p^+nSi/CoVO-2		4.96% V doped			SEM (Fig. 1a, b, d), TEM (Fig. 1e, f), *J-E* curve (Fig. 2a, 2b, 3c, 5, S7, S18), IPCE (Fig. 1c), *J-t* curve (Fig. 2d), EIS (Fig. 3a, S12), OCP (Fig. 3b), XPS (Fig. 4, S16, S17, Table S2), SEM (Fig. S3), UPS (Fig. S8), ECSA (Fig. S15)
p^+nSi/CoVO-3		7.76 % V doped			*J-E* curve (Fig. 2a, 3c, 5, S18), EIS (Fig. 3a), OCP (Fig. 3b), XPS (Fig. 4, S16, S17, Table S2), SEM (Fig. S3), ECSA (Fig. S15)
p^+nSi/CoO-14000s		Co_3O_4		14000 nm	EDX (Fig. 2), GIXRD (Fig. S5), *J-E* curves (Fig. S6), Raman (Fig. S14)
p^+nSi/CoVO-1-14000s		2.91 % V doped	$(Co+V)O_x$		EDX (Fig. 2), GIXRD (Fig. S5), *J-E* curves (Fig. S6)
p^+nSi/CoVO-2-14000s		4.96% V doped			EDX (Fig. 2), GIXRD (Fig. S5), *J-E* curves (Fig. S6), Raman (Fig. S14)
p^+nSi/CoVO-3-14000s		7.76 % V doped			EDX (Fig. 2), GIXRD (Fig. S5), *J-E* curves (Fig. S6)
nSi/CoVO-2-14000s	nSi	4.96% V doped			Electrical measurements (Fig. S10)
p^+Si/CoVO-2-14000s	p^+Si				
p^+nSi	p^+nSi				SEM (Fig. 1c)
p^+Si	p^+Si				UPS (Fig. S8)

[1] C. G. Morales-Guio, L. Liardet, X. Hu. Oxidatively Electrodeposited Thin-Film Transition Metal (Oxy)Hydroxides as Oxygen Evolution Catalysts. J Am Chem Soc. 138 (2016) 8946-57

[2] J. Yang, H. Liu, W. N. Martens, R. L. Frost. Synthesis and Characterization of Cobalt Hydroxide, Cobalt Oxyhydroxide, and Cobalt Oxide Nanodiscs. The Journal of Physical Chemistry C. 114 (2010) 111.

[3] B. Guo, T. Li, H. Hu. Anodic Deposition of Coooh Films with Excellent Performance for Electrochemical Capacitors. Journal of Applied Electrochemistry. 46 (2016) 403.

[4] X. Feng, W. Xing, L. Song, Y. Hu. In Situ Synthesis of a MoS_2/CoOOH Hybrid by a Facile Wet Chemical Method and the Catalytic Oxidation of Co in Epoxy Resin During Decomposition. Journal of Materials Chemistry A. 2 (2014) 13299.

[5] C. C. McCrory, S. Jung, J. C. Peters, T. F. Jaramillo. Benchmarking Heterogeneous Electrocatalysts for the Oxygen Evolution Reaction. J Am Chem Soc. 135 (2013) 16977.

[6] M. C. Biesinger, B. P. Payne, A. P. Grosvenor, L. W. M. Lau, A. R. Gerson, R. S. C. Smart. Resolving Surface Chemical States in XPS Analysis of First Row Transition Metals, Oxides and Hydroxides: Cr, Mn, Fe, Co and Ni. Applied Surface Science. 257 (2011) 2717.

[7] J. Yang, J. K. Cooper, F. M. Toma, K. A. Walczak, M. Favaro, J. W. Beeman, L. H. Hess, C. Wang, C. Zhu, S. Gul, J. Yano, C. Kisielowski, A. Schwartzberg, I. D. Sharp. A Multifunctional Biphasic Water Splitting Catalyst Tailored for Integration with High-Performance Semiconductor Photoanodes. Nat Mater. 16 (2017) 335.

[8] G. Xu, Z. Xu, Z. Shi, L. Pei, S. Yan, Z. Gu, Z. Zou. Silicon Photoanodes Partially Covered by Ni@$Ni(OH)_2$ Core-Shell Particles for Photoelectrochemical Water Oxidation. ChemSusChem. 10 (2017) 2897.

[9] Q. Cai, W. Hong, C. Jian, J. Li, W. Liu. Impact of Silicon Resistivity on the Performance of Silicon Photoanode for Efficient Water Oxidation Reaction. ACS Catalysis. 7 (2017) 3277.

[10] X. Zhou, R. Liu, K. Sun, K. M. Papadantonakis, B. S. Brunschwig, N. S. Lewis. 570 mV Photovoltage, Stabilized n-Si/CoO_x heterojunction Photoanodes Fabricated Using Atomic Layer Deposition. Energy Environ Sci. 9 (2016) 892.

[11] T. Yao, R. Chen, J. Li, J. Han, W. Qin, H. Wang, J. Shi, F. Fan, C. Li. Manipulating the Interfacial Energetics of N-Type Silicon Photoanode for Efficient Water Oxidation. J Am Chem Soc. (2016)

[12] L. Chen, J. Yang, S. Klaus, L. J. Lee, R. Woods-Robinson, J. Ma, Y. Lum, J. K. Cooper, F. M. Toma, L. W. Wang, I. D. Sharp, A. T. Bell, J. W. Ager. P-Type Transparent Conducting Oxide/N-Type Semiconductor Heterojunctions for Efficient and Stable Solar Water Oxidation. J Am Chem Soc. 137 (2015) 9595.

[13] K. Sun, M. T. McDowell, A. C. Nielander, S. Hu, M. R. Shaner, F. Yang, B. S. Brunschwig, N. S. Lewis. Stable Solar-Driven Water Oxidation to $O_2(G)$ by Ni-Oxide-Coated Silicon Photoanodes. J Phys Chem Lett. 6 (2015) 592.

[14] J. H. Yang, K. Walczak, E. Anzenberg, F. M. Toma, G. B. Yuan, J. Beeman, A. Schwartzberg, Y. J. Lin, M. Hettick, A. Javey, J. W. Ager, J. Yano, H. Frei, I. D. Sharp. Efficient and Sustained Photoelectrochemical Water Oxidation by Cobalt Oxide/Silicon Photoanodes with Nanotextured Interfaces. Journal of the American Chemical Society. 136 (2014) 6191.

[15] B. Mei, A. A. Permyakova, R. Frydendal, D. Bae, T. Pedersen, P. Malacrida, O. Hansen, I. E. Stephens, P. C. Vesborg, B. Seger, I. Chorkendorff. Iron-Treated Nio as a Highly Transparent P-Type Protection Layer for Efficient Si-Based Photoanodes. J Phys Chem Lett. 5 (2014) 3456.

[16] S. Hu, M. R. Shaner, J. A. Beardslee, M. Lichterman, B. S. Brunschwig, N. S. Lewis. Amorphous

TiO_2 Coatings Stabilize Si, Gaas, and Gap Photoanodes for Efficient Water Oxidation. Science. 344 (2014) 1005.